31st Congress of the International Council of the Aeronautical Sciences
Belo Horizonte, Brazil; September 09-14, 2018

CFD INVESTIGATION OF AERODYNAMIC COEFFICIENTS AND STALL CHARACTERISTICS FOR HIGH LIFT CONFIGURATIONS

Ricardo G. da Silva* , **Leonardo M. M. O. Carvalho**** , **Alexandre C. V. M. Almeida****
João Luiz F. Azevedo*
* **Instituto de Aeronáutica e Espaço, CTA/IAE/ALA, São José do Campos, SP, Brazil**
** **Instituto Tecnológico de Aeronáutica, DCTA/ITA, São José dos Campos, SP, Brazil**

Keywords: *High-Lift Configurations, CFD, Turbulence Modeling*

Abstract

The present work is concerned with the study of high-lift configurations. In particular, the JAXA Standard Model (JSM) configuration is adopted, because there are experimental data available for this configuration, both for the wing-body (WB) alone geometry as well as for the wing-body-pylon-nacelle (WBPN) configuration. Simulations are performed using a Reynolds-average Navier-Stokes formulation, augmented with the Spalart-Allmaras turbulence model. The computational tool is a standard, 2nd-order, cell-centered finite volume code for general unstructured meshes, which was developed in-house. Results for both WB and WBPN configurations are presented and these are able to reproduce the flow characteristics observed in the experimental data.

1 Introduction

Computational Fluid Dynamics (CFD) has become a quite mature science field due to many years of development. Nowadays, CFD is used for everyday jobs and in all design phases of an airplane, from conceptual design to certification, and even sometimes to solve problems in the operational phase of the aircraft. In other words, CFD applications spread in all phases of the aircraft lifecycle. The initial design of a high-lift system is typically addressed using CFD as the primary tool. During such initial design phase, it is desirable that the airplane stall characteristics are well understood, since modifications on wing design are still possible at this design phase. A deep understanding of all physical features present on such a flow is relevant, since the ultimate goal is optimizing the maximum lift coefficient for landing configuration or the lift over drag ratio for a takeoff configuration. The confluence of the boundary layers with wakes, shock waves interacting with boundary layers, separation due to adverse pressure gradient and complex vortex structures are, for instance, some of the flow features present in a typical simulation of high-lift configurations. These flow features, which are inherent to such complex geometries, make the prediction of the aerodynamic coefficients of high-lift devices a challenge even for the most sophisticated CFD software available today.

The present work addresses such complex flowfields using an in-house developed CFD solver. The main objectives of the present effort are, therefore, to benchmark our numerical tool against both experimental and computational data available in the literature as well as to improve our understanding of the issues involved in high-lift calculations over complex geometries. The present code, named BRU3D, solves the Reynolds-averaged Navier-Stokes (RANS) equations using a 2nd-order cell-centered finite volume method applied to general unstructured

grids. Since turbulence effects play an important role in predicting the flow behavior over high-lift configurations, as well as most relevant engineering applications in commercial aircraft, the formulation is closed with appropriate turbulence models. Several turbulence closures are available in the BRU3D code, but the present calculations have all used the Spalart-Allmaras (SA) turbulence model [1, 2]. It is important, as well, to mention that the meshes for these types of configurations are easily close to 100 million cells. In order to deal with such meshes, the code uses the FORTRAN 90 programming language allied with dynamic memory allocation and the Message Passing Interface (MPI) parallel paradigm.

The particular configuration addressed in the present work is the so-called JAXA Standard Model (JSM). This configuration has been studied in the 3rd AIAA CFD High Lift Prediction Workshop (HiLiftPW-3) and very detailed geometry information is available, as well as experimental data from wind tunnel tests. The organizing committee of HiLiftPW-3 has also made available several computational meshes for the JSM configuration. In particular, we have used the 100 million cell grid for the wing-body (WB) configuration and the 120 million cell mesh for the wing-body-pylon-nacelle (WBPN) configuration. These are the grids with the medium level of refinement available from the workshop website. The present effort is divided into two main lines of work. Initially, the capability of the present implementation of the SA model to capture the stall characteristics for the configurations with and without pylon and nacelle is considered. Afterwards, a comparison of lift coefficient (C_L), drag coefficient (C_D) and pitching moment (C_M) results, obtained with the present formulation, is performed against the wind tunnel results.

In the next sections, the numerical methodology used to solve the RANS equations are briefly presented, together with some indication of the compressible formulation for the Spalart-Allmaras turbulence model. In Section 4, the numerical results for the high-lift JSM configuration are compared with experimental results obtained from the 3rd AIAA CFD High Lift Prediction Workshop (HiLiftPW-3) website. Finally, some concluding remarks are presented, addressing some of the main observations that resulted from the present effort.

2 Theoretical and Numerical Formulation

The RANS equations are, in a mathematical context, a very complex set of equations to deal with. They consist of a system of nonlinear partial differential equations. In order to solve this system, in its discretized form, a numerical methodology has to be used. The BRU3D code does this task using an implicit time-stepping method for time march with numerical robustness and the Roe flux-difference splitting scheme [3] for spatial discretization. The turbulence closure used is the SA model [2]. In the next subsections, the Reynolds-averaged Navier-Stokes (RANS) equations, the Spalart-Allmaras turbulence model, and the numerical methodologies are briefly explained.

2.1 Reynolds-Averaged Navier-Stokes Equations

The 3-D compressible Reynolds-averaged Navier-Stokes (RANS) equations describe the flow, which is assumed to be fully turbulent. The averaging process adopted for compressible flow is the so-called Favre averaging. The Navier-Stokes equations, in their dimensional form, after the Favre averaging process, are given by

$$\frac{\partial Q}{\partial t} + \nabla \cdot (E_e - E_v) = 0 \,. \tag{1}$$

The vector of conserved quantities, Q, is given by

$$Q = [\rho \quad \rho u \quad \rho v \quad \rho w \quad e]^T \,, \tag{2}$$

in which ρ is the density, u, v, w are the velocity vector ($\mathbf{v}$) components and e is the total energy per unit volume, which is defined as

$$e = \rho \left[e_i + \frac{1}{2} \left(u^2 + v^2 + w^2 \right) \right] \,. \tag{3}$$

The inviscid (E_e) and viscous (E_v) flux vectors can be written as

$$E_e = \begin{Bmatrix} \rho \mathbf{v} \\ \rho u \mathbf{v} + p\hat{i}_x \\ \rho v \mathbf{v} + p\hat{i}_y \\ \rho w \mathbf{v} + p\hat{i}_z \\ (e+p)\mathbf{v} \end{Bmatrix} \tag{4}$$

$$E_v = \begin{Bmatrix} 0 \\ \left(\tau^l_{xj} + \tau^t_{xj}\right)\hat{i}_j \\ \left(\tau^l_{yj} + \tau^t_{yj}\right)\hat{i}_j \\ \left(\tau^l_{zj} + \tau^t_{zj}\right)\hat{i}_j \\ \beta_j \hat{i}_j \end{Bmatrix} \tag{5}$$

In the previous equations, the viscous stress tensor, τ^l_{ij}, is defined as

$$\tau^l_{ij} = \mu_l \left(\frac{\partial u_i}{\partial x_j} + \frac{\partial u_j}{\partial x_i} - \frac{2}{3}\frac{\partial u_m}{\partial x_m}\delta_{ij} \right) . \tag{6}$$

Here, u_i represents the velocity components, and x_i refers to the coordinate of the Cartesian system. The dynamic viscosity coefficient, μ_l, is calculated using the Sutherland law in the present work. The static pressure, p, is given by the perfect gas law, which has the form

$$p = (\gamma - 1)\left[e - \frac{1}{2}\left(u^2 + v^2 + w^2\right) \right] . \tag{7}$$

The term that includes the work done by the viscous forces and, also, the heat conduction vector, which is indicated by β_j in the previous equations, is defined as

$$\beta_j = \left(\tau^l_{ji} + \tau^t_{ji}\right) u_i - q_j . \tag{8}$$

Moreover, the components of the heat conduction vector are calculated as

$$q_j = -\gamma \left(\frac{\mu_l}{Pr} + \frac{\mu_t}{Pr_t} \right) \frac{\partial (e_i)}{\partial x_j} . \tag{9}$$

Here, Pr is the Prandtl number and Pr_t is the turbulent Prandtl number, which are assumed constant in the present calculations.

The unknown Reynolds stress tensor, τ^t, is modeled by different turbulence models within the BRU3D code, including linear and nonlinear eddy viscosity models, as well as Reynolds stress closures. In the present effort, however, as already discussed, the Spalart-Allmaras closure [1, 2] is used and, hence, the components of the Reynolds stress tensor can be written assuming a linear eddy viscosity relation as

$$\tau^t_{ij} = \mu_t \left[\left(\frac{\partial u_i}{\partial x_j} + \frac{\partial u_j}{\partial x_i} \right) - \frac{2}{3}\frac{\partial u_m}{\partial x_m}\delta_{ij} \right] - \frac{2}{3}\rho k \delta_{ij} . \tag{10}$$

Here, k is the turbulent kinetic energy and μ_t is the eddy viscosity coefficient. In our case, the term related to k is incorporated by the pressure, once the turbulence model selected does not have an explicit relation for k. The transport equation used for the SA model is presented in Sec. 2.2.

The RANS equations, together with the turbulence model equation, are discretized using a cell-centered finite volume method. These equations, after spatial discretization, can be written as

$$V_i \frac{\partial Q_i}{\partial t} = -\sum_{k=1}^{nf} \left(E_{e_k} - E_{v_k}\right) \cdot S_k = -RHS , \tag{11}$$

where the k subscript indicates properties computed in the k-th face, and nf represents the number of faces which form the i-th control volume. In order to obtain Eq. (11), we consider a constant flux through volume faces and, also, constant Q_i properties inside the control volume. The first assumption is a sufficient approximation to obtain 2nd-order accuracy with the currently available flux computation schemes. In the convective flux computation, a Roe flux-difference splitting scheme [3] is used. In order to achieve 2nd-order accuracy in space, primitive properties are linearly reconstructed at cell faces with the MUSCL algorithm [4]. In order to maintain adequate resolution across discontinuities, the variable reconstruction is affect by limiter functions, such as the Venkatakrishnan, minmod, van Albada or SuperBee limiters, which are all currently available in the BRU3D code. The present effort uses the Venkatakrishnan limiter [5]. In addition, the viscous terms are discretized using a method that

computes nonoscillatory derivatives at the cell faces.

A 1st-order backward Euler implicit scheme for Eq. 11 is given by

$$V_i \frac{\Delta Q_i^n}{\Delta t} = -RHS\left(Q_i^{n+1}\right) . \tag{12}$$

Here, $\Delta Q_i^n = Q_i^{n+1} - Q_i^n$. The linearization uses an expansion of $RHS\left(Q_i^{n+1}\right)$ about ΔQ_i^n as

$$RHS\left(Q_i^{n+1}\right) = RHS\left(Q_i^n\right) + \frac{\partial RHS\left(Q_i^n\right)}{\partial Q_i^n}\Delta Q_i^n + O\left(\Delta Q_i^n\right)^2 \tag{13}$$

and leads to the 1st-order accurate implicit scheme

$$V_i \frac{\Delta Q_i^n}{\Delta t} + \frac{\partial RHS\left(Q_i^n\right)}{\partial Q_i^n}\Delta Q_i^n = -RHS\left(Q_i^n\right) . \tag{14}$$

More details on the calculation of the residue, $\left(RHS\left(Q_i^n\right)\right)$, the Jacobian matrix, $\left[\frac{\partial RHS\left(Q_i^n\right)}{\partial Q_i^n}\right]$, and the fluxes can be found in Ref. [6].

2.2 Spalart-Allmaras Model

The Spalart-Allmaras model [2] is a one-equation model, which is written for a modified kinematic eddy viscosity, $\tilde{\nu}$. This is a widely used closure by the aerospace community. The transport equation of the SA model, in its compressible version, is given by

$$\begin{aligned} &\frac{\partial(\rho\tilde{\nu})}{\partial t} + \frac{\partial(\rho u_j\tilde{\nu})}{\partial x_j} = \\ &\rho c_{b1}\hat{S}\tilde{\nu} - \rho c_{w1} f_w \left(\frac{\tilde{\nu}}{d}\right)^2 + \\ &+\frac{1}{\sigma}\left[\frac{\partial}{\partial x_j}\left(\rho\left(\nu+\tilde{\nu}\right)\frac{\partial\tilde{\nu}}{\partial x_j}\right) + \rho c_{b2}\frac{\partial\tilde{\nu}}{\partial x_i}\frac{\partial\tilde{\nu}}{\partial x_i}\right] \\ &-\frac{1}{\sigma}\left(\nu+\tilde{\nu}\right)\frac{\partial\rho}{\partial x_i}\frac{\partial\tilde{\nu}}{\partial x_i} \end{aligned} \tag{15}$$

The first and second trip terms are left out from Eq. (15). The turbulent eddy viscosity coefficient is obtained from

$$\mu_t = \rho\tilde{\nu} f_{v1} , \tag{16}$$

where $f_{v1} = \frac{\chi^3}{\chi^3 + c_{v1}^3}$, $\chi = \frac{\tilde{\nu}}{\nu}$. In order to avoid $\tilde{S}$ to become negative, a limiting method is used, which can be expressed as

$$\hat{S} = \begin{cases} \Omega + \overline{S} & \text{if } \overline{S} \geq -c_2\Omega \\ \Omega + \frac{\Omega(c_2^2\Omega + c_3\overline{S})}{(c_3 - 2c_2)\Omega - \overline{S}} & \text{if } \overline{S} < -c_2\Omega \end{cases} \tag{17}$$

$$\overline{S} = \frac{\hat{\nu}}{\kappa^2 d^2} f_{v2} . \tag{18}$$

Here, d is the distance from cell center to nearest wall and $\kappa = 0.41$ is the von Kármán constant. The $\Omega = \sqrt{2W_{ij}W_{ij}}$ term is the magnitude of the antisymmetric part of the velocity gradient tensor. Moreover, the antisymmetric tensor is computed from $W_{ij} = \frac{1}{2}\left(\frac{\partial u_i}{\partial x_j} - \frac{\partial u_j}{\partial x_i}\right)$. The others variables and functions, which are found in Eq. (15), are given by

$$f_{v2} = 1 - \frac{\chi}{1 + \chi f_{v1}} , \tag{19}$$

$$f_w = g\left[\frac{1 + c_{w3}^6}{g^6 + c_{w3}^6}\right]^{1/6} , \tag{20}$$

$$g = r + c_{w2}\left(r^6 - r\right) , \tag{21}$$

$$r = \min\left[\frac{\tilde{\nu}}{\tilde{S}\kappa^2 d^2}, 10\right] . \tag{22}$$

The constants are $c_{b1} = 0.1355$, $c_{b2} = 0.622$, $\sigma = \frac{2}{3}$, $c_{w2} = 0.30$, $c_{w3} = 2$, $c_{v1} = 7.1$, $c_2 = 0.7$ and $c_3 = 0.9$. This new equation is solved fully coupled with the RANS equations. The production, destruction and cross-diffusion terms present in Eq. (15) are treated implicitly. Thus, the Jacobian matrices for these terms are also calculated.

3 The JSM Model

The geometry that is under study in the present case is the JAXA Standard Model (JSM) high-lift configuration [7]. This wind-tunnel model represents a mid-sized airliner jet, conceptualized from scratch by JAXA. The preliminary design constraints were established as follows. The maximum take-off weight of 100,000 lbs, cruising and maximum Mach numbers of 0.8 and 0.84,

respectively, cruising range of 2300 nm, landing distance of 4000 ft and take-off distance of 5000 ft.

The half-span wind-tunnel model, seen in Fig. 1, represents the configuration developed by JAXA, in its complete assembly. It has a circular fuselage, flap track fairings (FTF), pylon, nacelle and high-lift devices. The general model dimensions include a 2.3 m half-span and 4.9 m of fuselage length. Other important model dimensions are described in Tab. 1. The JSM configuration is the high-lift system that is addressed here in a nominal landing configuration with support brackets on, and pylon/nacelle on and off. The experiment used a semi-span model with a 60 mm peniche standoff, but the present computations are performed in "free air", *i.e.*, without the wall test section and the semi-span effects.

Table 1 Important dimensions of the JSM model.

Important Dimensions of the JSM model	
Half span lengh	2.3 m
Mean aerodynamic chord	0.5292 m
Wing area (half span)	1.233 m^2
Sweep angle	33 deg.
Aspect ratio	9.42
Taper ratio	0.333

Fig. 1 JAXA model in its full configuration [7].

Experimental results for the aerodynamic coefficients are available on 3rd AIAA CFD High Lift Prediction Workshop (HiLiftPW-3) website. The lift, drag and pitching moment coefficients were obtained from a wind tunnel run at Reynolds number equal to 1.93 million, based on the wind tunnel model mean aerodynamic chord, and Mach number equal to 0.172. The pressure coefficient distributions for several sections along the JSM model wing spam are also available. However, C_p data is not used in the present effort. In addition, oil flow visualizations were performed and, hence, such information is also available in the website. This type of visualization is very useful to identify separation regions over the wing, which are directed related to stall characteristics of aircraft configurations. Moreover, the numerical shear-stress lines on the model surface can be directly compared with oil flow visualizations. All the available data is related to configurations with nacelle/pylon on and off.

The meshes used here for both WB and WBPN configurations are hybrids meshes, which means that they are composed of prismatic cells in the near wall region, which gives them a better representation of the boundary layer, and the rest of computational domain is filled with combinations of pyramidal and tetrahedral cells. The meshes have significant grid refinement at the wing wake region. The particular set of meshes used here are available on the HiLiftPW-3 website with the name of JSM_UnstrMixed_ANSA. Moreover, these meshes are classified as medium refinement level grids. The WB configuration mesh has 109 million cells and the WBPN grid has 120 million cells.

4 Results

The numerical results obtained with the BRU3D code are presented and compared with experimental data. The flow condition considered is identical to that of the experimental data, *i.e.*, $M_\infty = 0.172$ and Reynolds number equal to 1.93 million. The experimental results presented are based on data with and without corrections. The corrections try to eliminate wind tunnel wall ef-

fects and semi-spam effects.

Figure 2 presents the lift curve, drag polar and pitching moment curve for JSM–WB configuration. The present results are indicated by the red symbols, whereas the dark blue symbols represent the correct wind tunnel data and the light blue symbols indicate the raw or uncorrected experimental data. It is possible to observe from Fig. 2(a) that there is good agreement between numerical and experimental results of lift coefficient for angles of attack up to 10.47 deg. However, for angles of attack larger than 10.47 deg., the lift coefficient is underestimated. Moreover, the stall occurs earlier in the numerical results. It occurs at 18.58 deg. for the present numerical results and around 20 deg. for the experimental data. Fig. 2(b) presents the drag polar. The comparison also shows that, although the present calculations follow the correct trends of the experimental data, it possible to observe differences between the two sets of results. The pitching moment distributions, shown in Fig. 2(c), also present good agreement with the experimental results for angles of attack up to 10.47 deg. For angles of attack larger than that, the results present a discrepancy that increases as the lift coefficient also increases. This behavior can be related to the numerical stall characteristics predicted for the present configuration.

Figures 3 and 4 show the comparison of oil flow visualizations from the wind tunnel tests with the computational shear-stress lines of JSM–WB configuration for angles of attack equal to 18.58 deg. and 21.57 deg., respectively. The lower angle represents a flight condition prior to the stall angle of attack. In this case, the shear-stress lines, shown in Fig. 3(b) present patterns which are similar to the oil flow patterns, shown in Fig. 3(a). It is possible to identify, in Figs. 3(a) and 3(b), the presence of the horseshoe vortex in the wing-body junction, the flow separation at the wing tip and, also, the effects of slat brackets.

The other test case, *i.e.*, at the higher angle of attack, is above the stall condition for both experiment and computation. Therefore, one can see in Fig. 4 that the agreement between computational and experimental results is not as good. For instance, at the inboard region of the wing, the effects of the horseshoe vortex seem to be stronger

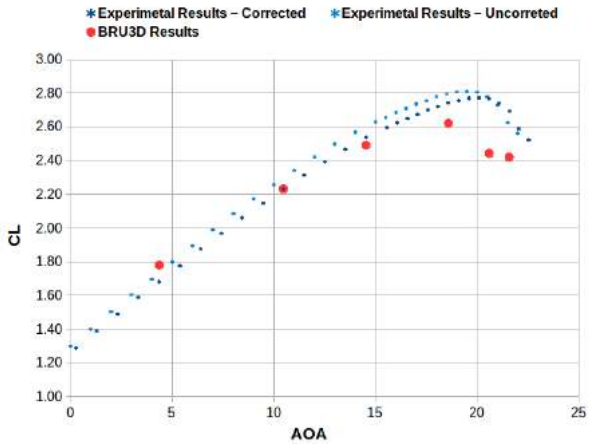

(a) Lift Curve

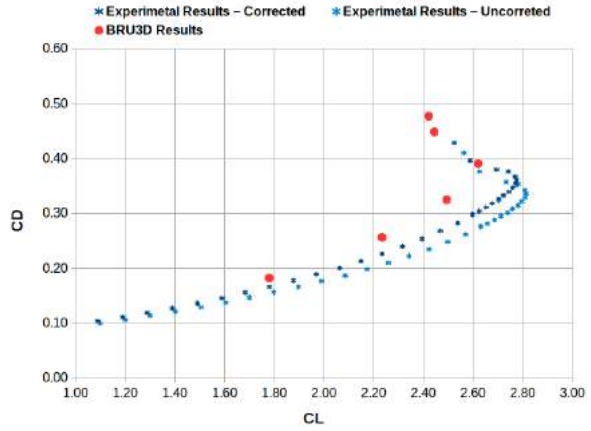

(b) Drag Polar

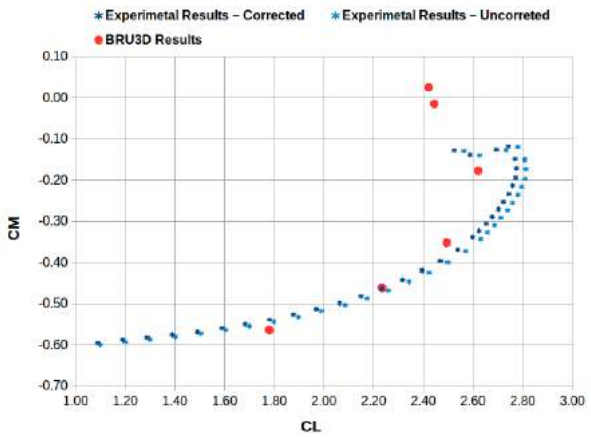

(c) Pitching Moment Curve

Fig. 2 Aerodynamic coefficients for JSM–WB configuration.

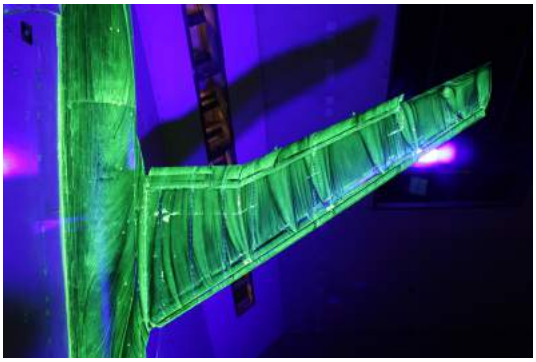

(a) Experimental data: Oil flow visualization.

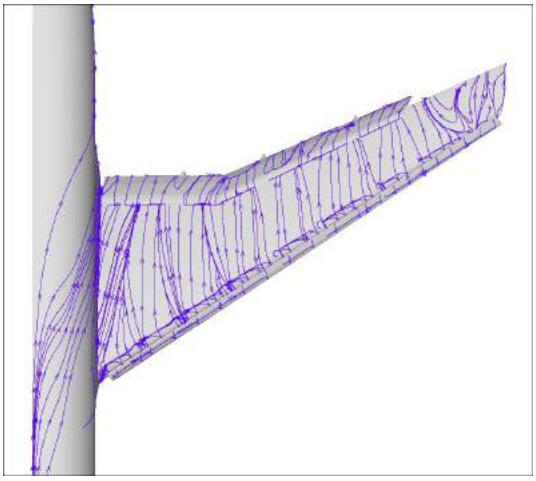

(b) Numerical results: Shear-stress lines.

Fig. 3 Comparison of oil flow visualization and shear-stress lines for JSM–WB at $\alpha = 18.58$ deg.

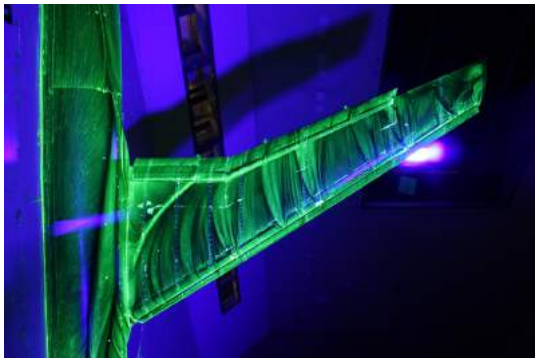

(a) Experimental data: Oil flow visualization

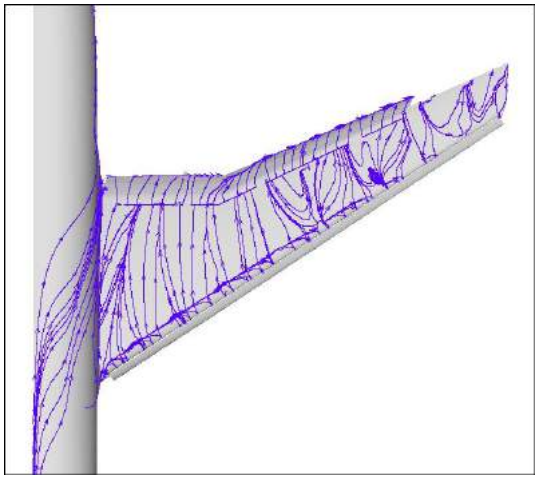

(b) Numerical results: Shear-stress lines

Fig. 4 Comparison of oil flow visualization and shear-stress lines for JSM–WB at $\alpha = 21.57$ deg.

in the experimental data than in the numerical results. Moreover, the numerical results seem to indicate that there is some flow separation around midspan of the wing. Hence, experimental data indicate that stall is triggered by the horseshoe vortex at the wing root, whereas stall seems to start further outboard along the wingspan for the computational results. In this latter case, stall seems to be triggered by the slat brackets. On the other hand, it should be noted that, for this angle of attack, the flow patterns observed at the wing tip are similar for experimental and numerical results.

Figure 5 shows the lift curve, drag polar and the pitching moment curve for the JSM–WBPN configuration. The lift coefficient results, shown in Fig. 5(a), obtained from the computations have good agreement with the experimental data throughout most of the angle-of-attack range considered. The exception is, again, around the stall angle of attack. However, it is interesting that, although the present computations still underpredict $C_{L_{max}}$ and the stall angle of attack, the agreement in this case is better than the one observed for the WB configuration. The numerical results for the drag polar captured the behavior of experimental data, as one can see in Fig. 5(b). However, the shift between numerical and experimental drag results is large enough to indicate that an improvement in mesh refinement is necessary. The numerical results for the pitching moment coefficient also present a similar behavior to the experimental data for angles of attack smaller than 20.59 deg., which is the stall angle

of attack. This comparison is seen in Fig. 5(c), in which the pitching moment is presented as a function of the lift coefficient.

Figures 6 and 7 present the comparison between oil flow visualizations and shear-stress lines for the JSM–WBPN configuration for angles of attack equal to 18.58 and 21.57 deg., respectively. For $\alpha = 18.58$ deg., the observed pattern of the shear-stress lines is almost identical to the one observed for the oil flow visualization. It is possible to identify, in Fig. 6, the horseshoe vortex, the effects of the nacelle wake, both for its inboard and outboard portions, and the wing tip separation. All of these flow futures are present in both experimental and numerical results. The effects of horseshoe vortex, in the numerical results, seem to be a bit stronger than in the experimental data. On the other hand, the nacelle wake effects for the numerical results seem to be weaker than what is observed in the experimental data. The wing tip separated region, observed in experimental data, is somewhat smaller than the region of separated flow observed in the numerical results for the wing tip.

For the higher angle of attack, *i.e.*, $\alpha = 21.57$ deg., with the visualizations shown in Fig. 7, it is possible to identify the horseshoe vortex footprint at the wing-body junction region, the nacelle wake effects on the main wing element, the effects of the slat supports, and the wing tip separation. As before, this is true for both experimental and numerical results. From the oil flow visualization and shear-stress lines, and contrary to what was discussed for the lower angle of attack, it is possible to infer that the horseshoe vortex effects are stronger in the experiments than in the computational results. On the other hand, the wing tip separation region, predicted by the calculations, is larger than the one seen in the experimental data. The nacelle wake seems to have similar effects on the upper surface of the wing for both experimental and numerical results.

At the outboard regions of the wing, as we have seen for all computational results here presented, there is a considerably large separation region. The present numerical code is not the only one to indicate this flow feature for this con-

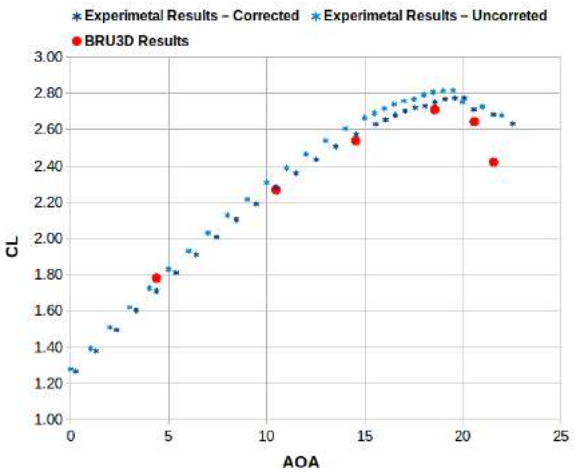

(a) Lift Curve

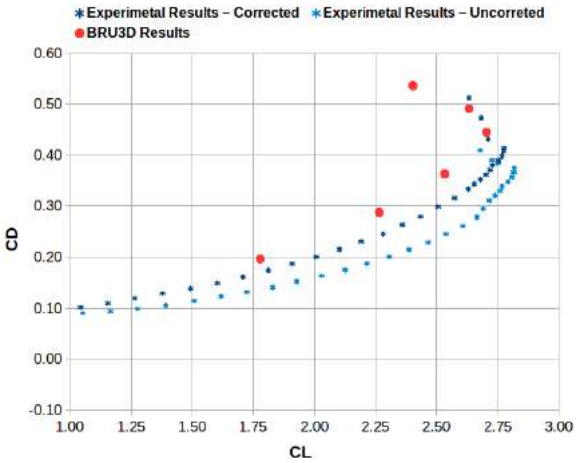

(b) Drag Polar

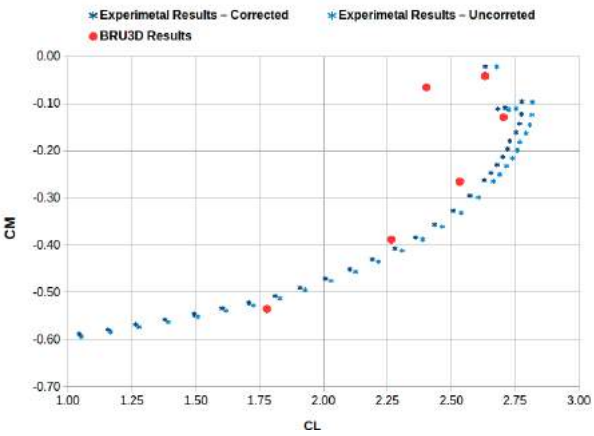

(c) Pitching Moment Curve

Fig. 5 Aerodynamic coefficients for JSM–WBPN configuration.

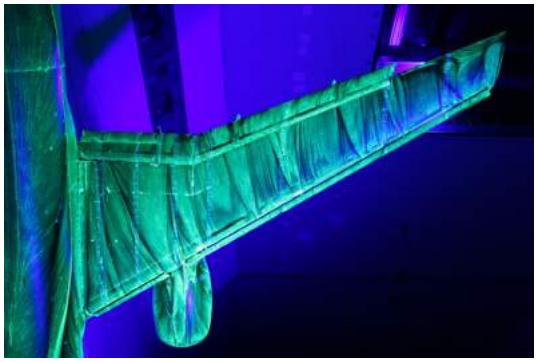

(a) Experimental data: Oil flow visualization

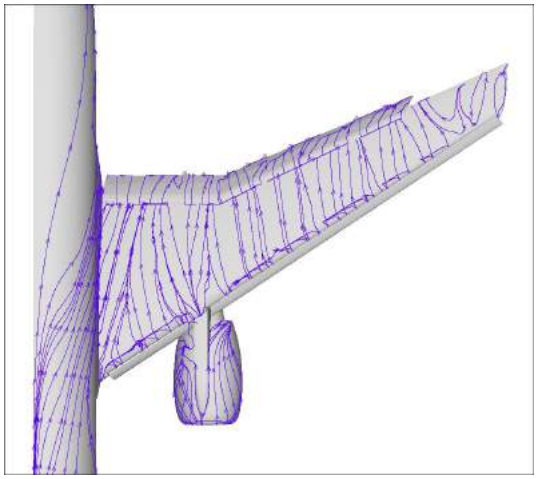

(b) Numerical results: Shear-stress lines

Fig. 6 Comparison of oil flow visualization and shear-stress lines for JSM–WBPN at $\alpha = 18.58$ deg.

(a) Experimental data: Oil flow visualization

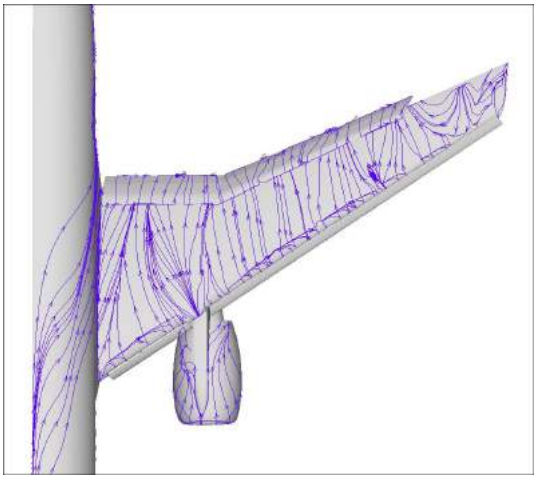

(b) Numerical results: Shear-stress lines

Fig. 7 Comparison of oil flow visualization and shear-stress lines for JSM–WBPN at $\alpha = 21.57$ deg.

figuration at high angles of attack. It is possible that the numerical calculations are seeing some hyper-sensitivity to the effects of the slat brackets, since the experimental data show, in the same region, some affects of the slat bracket wakes, but not a separation region. It is important, however, to emphasize that such flow feature is not triggering the stall for the WBPN configuration. The stall for numerical simulations, and also for experimental results, seems to be triggered by a combination of the wing-body junction horseshoe vortex and the nacelle wake. These features interact over the upper surface of the main wing element and, eventually, lead to the stall condition.

5 Concluding Remarks

In the present work, we perform numerical simulations for a standard high-lift configurations, which is being used by the community as a form of evaluating the capability of CFD codes to capture the complex flow features present on typical take-off and landing airliner configurations. In particular, the JAXA Standard Model (JSM) configuration was addressed, both for the wing-body (WB) and the wing-body-pylon-nacelle (WBPN) cases. The CFD code used in the present calculations is an in-house developed tool, which solves the Reynolds-averaged Navier-Stokes equations together with the Spalart-Allmaras turbulence model. It is a 2nd-order, cell-centered, finite vol-

ume code for general unstructured grids. For the WB configuration, a 100 million cell mesh is used, whereas the grid for the WBPN case had 120 million cells. For both JSM configuration, the comparisons between experimental and numerical results show that there is good agreement for all aerodynamics coefficients while the flow remains attached.

The experimental results of JSM–WB configuration indicate that stall is triggered by the horseshoe vortex at the wing root. However, the numerical results are indicating that stall starts further outboard along the wingspan. For the JSM–WBPN configuration both numerical and experimental results show similar stall characteristics, *i.e.*, that stall starts as a consequence of the interaction of the wing-body junction horseshoe vortex and the nacelle wake separation. Moreover, the wake of slat support brackets seem to have a considerable effect on the numerical results, especially towards the wing tip, creating a fairly large separation region. This effect was also observed in other numerical codes.

6 Acknowledgments

The authors gratefully acknowledge the support for the present research provided by Conselho Nacional de Desenvolvimento Científico e Tecnológico, CNPq, under the Research Grant No. 309985/2013-7. The work is also supported by Fundação de Amparo à Pesquisa do Estado de São Paulo, FAPESP, under the Research Grants No. 2013/07375-0 and No. 2016/50477-6. The support provided by CNPq, through a graduate scholarship for the second author, is also greatly appreciated.

References

[1] Spalart P. and Allmaras S., A One-Equation Turbulence Model for Aerodynamic Flows, *Proceedings of the 30th AIAA Aerospace Sciences Meeting and Exhibit*, Reno, NV, 1992.

[2] Spalart P. and Allmaras S., A One-Equation Turbulence Model for Aerodynamic Flows, *Recherche Aerospatiale*, Vol. 7, No. 1, 1994, pp. 5-21.

[3] Roe P. L., Approximatte Riemann Solvers, Parameter Vectors, and Difference Schemes, *Journal of Computational Physics*, Vol. 43, No. 2, 1981, pp. 357-372.

[4] van Leer B., Towards the Ultimate Conservative Difference Scheme. V. A Second-Order Sequel to Godunov's Method, *Jornal of Computational Physics*, Vol. 32, No. 1, 1979, pp. 101-136.

[5] Venkatakrishnan V., On the Accuracy of Limiters and Convergence to Steady State Solution, *Proceedings of the 31st AIAA Aerospace Sciences Meeting and Exhibit*, Reno, NV, 1993.

[6] Bigarella E. D. V. and Azevedo J. L. F., A Unified Implicit CFD Approach for Turbulent-Flow Aerospace-Configuration Simulations, *Proceedings of the 47th AIAA Aerospace Sciences Meeting Including The New Horizons Forum and Aerospace Exposition*, Orlando, FL, 2009.

[7] Yokokawa Y., Murayamama M., Uchida H., Tanaka K., Ito T., and Yamamoto K., Aerodynamic Influence of a Half-Span Model Installation for High-Lift Configuration Experiment, *Proceedings of the 48th AIAA Aerospace Sciences Meeting Including The New Horizons Forum and Aerospace Exposition*, Orlando, Florida, 2010.

Contact Author Email Address

Mail to: ri_galdino@yahoo.com.br
Mail to: joaoluiz.azevedo@gmail.com

Copyright Statement